

Hexagonal $\text{Sr}_{0.6}\text{Ba}_{0.4}\text{MnO}_3$ Room Temperature Magneto-electric: Field Tunable Tunneling State and Entangled Pseudospin Clusters

Ritu Rawat¹, R.J. Choudhary^{1*}, A.M. Awasthi^{1*}, Archna Sagdeo², A.K. Sinha², Rajamani Raghunathan¹, V.G. Sathe¹, and D.M. Phase¹

¹UGC DAE Consortium for Scientific Research, Indore- 452 001, India

²Indus Synchrotrons Utilization Division, Raja Ramanna Centre for Advanced Technology, Indore- 452 013, India

Abstract

Hexagonal $\text{Sr}_{0.6}\text{Ba}_{0.4}\text{MnO}_3$ undergoes ferroelectric (FE) and antiferromagnetic (AFM) orderings having competing energetics within a narrow range close to the room temperature. Magnetic properties appear to be governed by intricate exchange interactions among Mn⁴⁺ ions within and in adjacent Mn_2O_9 bioctahedra, contingent upon local structural changes. Calculations based on our model spin-Hamiltonian reveal that the linear AFM fluctuations between the Mn⁴⁺ ions of two oxygen-linked bi-octahedra result in short range correlations, manifest as a smooth drop in magnetization below 325 K. On the other hand, the non-linear intra-bioctahedral Mn-O-Mn AFM interactions, which get enhanced and acquire long-range character below 225 K, cause a slope-break in magnetization vs. temperature. Consequently, dual magneto-electric effects are obtained, as the high-temperature soft mode FE phase first transforms below 325K into a tunneling state, and then crosses over into a reentrant cluster glass phase around ~ 225 K. Vitreous character of the electrical cluster glass phase is examined by the indispensable aging and rejuvenation effects, similar to the spin glasses. Field tunability of non-FE regimes, defining pseudospin composites of entangled spin and dipole, offers a prototype for room temperature atypical magneto-electricity. Frustration-competition involving spin-exchange and local-strain is reckoned as responsible for the dual/ \pm ve nature of magneto-electricity obtained in adjacent temperature regimes.

Keywords: multiferroics, magneto-electric, cluster glass

*Corresponding Authors: ram@csr.res.in, amawasthi@csr.res.in

In recent years, in some magneto-electric materials including cubic $\text{Sr}_{1-x}\text{Ba}_x\text{MnO}_3$, the prerequisite of d^0 -ness is not enforced for ferroelectricity (FE) [1-6]. Rather, the FE-origin in them is attributed to particulate atomic displacements responsible for the inversion-symmetry breaking, softening the appropriate phonon modes—which couple with the magnetic ordering in the material [7, 8]—thus realizing a novel mechanism for magneto-electricity. First principles calculations on TbMnO_3 featuring larger ionic-displacements of Mn^{3+} and Tb^{3+} (vs. oxygen's) have adequately explained its observed FE polarization magnitude [9, 10]. Ferroelectricity in cubic $\text{Sr}_{1-x}\text{Ba}_x\text{MnO}_3$ is induced due to the z -displacement of Mn^{4+} ion and modulation in O-Mn-O bond angle, because of the different ionic radii of Ba and Sr. For half-doped cubic $\text{Sr}_{1/2}\text{Ba}_{1/2}\text{MnO}_3$, though the ferroelectric transition is observed at $\sim 400\text{K}$, magneto-electricity occurs at and below the Néel temperature $T_N \sim 185\text{K}$ [6].

In this study we unravel the manifestation of ferroelectric and antiferromagnetic orderings in hexagonal $\text{Sr}_{0.6}\text{Ba}_{0.4}\text{MnO}_3$ (SBMO) within a narrow ambient range close to the room temperature. The resultant coupling of magnetic, electrical, structural, and vibrational degrees of freedom is experimentally established, along with recognition of peculiar electrical phases displaying novel magneto-electricity (ME). It is observed that while the global-structure remains the same, Mn-ion and oxygen-ions shift in position due to the strain applied by the doped Ba-ion, leading to elongation of the two Mn-O bond lengths (albeit differently), causing polarization. In antiferromagnetic regimes, non-ferroelectric/cooperative pseudospin (entangled spin- & dipole-composite, [11]) phases are found field-tunable. The present study places SBMO amongst the rare materials whose magnetic and electrical anomalies are both close to room temperature; hence it possesses a tremendous potential for magneto-electric functionality.

Polycrystalline hexagonal $\text{Sr}_{0.6}\text{Ba}_{0.4}\text{MnO}_3$ (SBMO) was prepared using solid state reaction method. Purity of the sample is confirmed using X-ray diffraction measurements and Rietveld and Le Bail fitting. X-ray diffraction measurements were performed using table top D2 phaser Bruker X-Ray diffractometer. An energy dispersive analysis of X-ray (EDAX) unit attached to FEI NOVA Nano SEM 450 was used to record EDAX pattern. Near edge X-ray absorption spectra was recorded at SXAS beamline BL-1, Indus-2, RRCAT, Indore. Raman measurements were performed using a HR800 Jobin-Yvon spectrometer. He-Ne laser with a wavelength of 632.8 nm was used to record Raman spectra in the temperature range of 90K to

450K. Magnetization measurement was carried out using 7T SQUID VSM (Quantum Design, USA). Dielectric measurements over 10Hz to 1MHz were performed in the temperature range of 100K to 430K in cooling cycle using Alpha-A high performance frequency analyzer (Novo Control). Specific heat $C_p(T)$ was obtained at 5°C/min warm up rate from STAR^E DSC-1 (Differential Scanning Calorimeter, Mettler-Toledo). Temperature dependent XRD measurements were performed using Synchrotron source at RRCAT Indus-2, BL-12. Field dependent isothermal magneto-dielectric measurements at 1kHz|_{210K} and 1MHz|_{300K} were performed using Alpha-A high-performance frequency analyzer (Novo Control) and a 9Tesla Integra cryostat/magnet (Oxford NanoSystems).

XRD analysis of the SBMO sample with Rietveld refinement and Le Bail fitting performed using Full Prof software confirms its single phase nature with hexagonal P6₃/mmc symmetry (shown in Fig. 1(a)) [12, 13]. EDAX measurement confirmed the stoichiometry of SBMO (shown in Fig. 1(b)). We have also carried out X-ray absorption spectroscopy (XAS) studies at Mn-L edge of SBMO, as shown in Fig. 1(c). The Mn-L edge feature contains L3 and L2 features due to spin-orbit coupling. The edge position and features of Mn-L edge, when compared with the reference sample MnO₂, also confirm the 4+ state of Mn, consistent with the stoichiometric oxygen content in the system. Magnetization measurements reveal two magnetic anomalies at $T_1 = 325\text{K}$ and $T_2 = 227\text{K}$. Linear M - H behavior [12] (not shown here) below both these benchmark temperatures evidences antiferromagnetic character below the room temperature. In SBMO, two face-shared MnO₆ octahedra stacked along the c -axis form bi-octahedral Mn₂O₉. This gives rise to two Mn-O-Mn interactions; a 180° linear Mn-O1-Mn (J_1) and another non-linear Mn-O-Mn (J_2) (bond angle 78.36°, as estimated from the analysis of the XRD pattern, Fig. 1(d)). Both the observed anomalies are due to alterations in local structure, affecting the superexchange interactions in both these networks [12]. The two anomalies are further confirmed by fitting magnetization with spin-Hamiltonians for separate temperature regimes, as discussed later in the manuscript in detail.

To establish the bona fides of the dielectric data on our ceramic specimen, we first examine and isolate the ω - T ranges of its main contributions. As the losses ($\epsilon'' = \sigma'/\epsilon_0\omega$) from various channels simply add up; vis-à-vis bulk, the extrinsic conductivity due to electrode surface layer and grain-boundaries dominates at low- ω and high- T , having its stronger thermal

activation character ($\sigma' \sim e^{-E_a/k_B T}$, with $E_a^{ext} > E_a^{int}$) and slower frequency dependence ($1/\tau^{ext} < 1/\tau^{int}$) [14, 15]. Therefore, to carry out a worst case analysis, we select our room temperature data, taken over a moderately broad frequency range (1Hz-1MHz). At room temperature, no relaxation loss-peak (in ε'' or $\tan\delta$) is observed—which appears to be shifted up and out of our measurement frequency range—therefore, we employ the ac-transport representation for the purpose. To this end, the complex impedance Nyquist plot is shown in Fig.2, with full range in the main-panel and its low-frequency zoom in the right-inset. From the clearly tri-sectioned behavior of the Nyquist plot, we immediately discern that the ‘linear’ Z'' vs. Z' regimes are due to the responses attributed to electrode surface layer (sample-boundary) for $f \lesssim 60\text{Hz}$, and to the grain-boundary for $f \lesssim 1\text{kHz}$. Their origin is the nearly constant/dispersion-free conductivity (left inset/right y -axis, with $\sigma' \gg \sigma''$), where the ‘constant’ slopes of $Z''(Z')$ at low frequencies directly relate to the ‘power-law’ manifestations of $\tan\delta(\omega)$ — $\Delta Z''/\Delta Z' \propto [d\log(\tan\delta)/d\log\omega]$. Typically large losses ($Z'/Z'' = \sigma'/\sigma'' = \varepsilon''/\varepsilon' \gg 1$) here characterize the two extraneous contributions. The ‘linear’ Z'' vs. Z' regimes signify the well-known ‘constant phase element’ [16] feature of our room temperature dielectric data, as also shown in the left inset (left y -axis). Furthermore, the higher-frequency impedance (Z^*) traces out a semicircle and dispersive conductivity follows the Jonscher power-law (left inset/right y -axis); $\sigma_{tot}^b(\omega) = \sigma_{dc}^b[1 + (\omega/\omega_h)^n]$, reflecting the bulk response. Therefore, the room temperature ac-response above $\sim O(\text{kHz})$ is rigorously delineated as predominantly intra-grain, and can thus be safely treated as intrinsic. The extrinsic/intrinsic crossover frequency downshifts at lower temperatures; e.g., by some two orders of magnitude at 150K.

Dielectric constant $\varepsilon'(T)$ (Fig. 3(a)) shows a peak at $\approx 355\text{K}$ (marked P1, which is frequency-indifferent up to $\pm 3\text{K}$)—evidencing a “quasi-local FE” transition for SBMO. Specific heat (C_p-T , inset) also clearly depicts a wide peak at 357K near the Curie temperature T_C . About $\sim 130\text{K}$ below P1, slopes of decreasing $\varepsilon'_\omega(T)$ steepen with frequency dependent shoulders (marked as P2, close to T_2). Plotted on the logarithmic scale (Fig. 3(b)), the dielectric constant is seen to enter a ‘plateau’ region some $\sim 30\text{K}$ below P1 (for all ω 's), which lasts down to P2. In $d\varepsilon'/dT$ plot (inset of Fig. 3(b)), two sets of peaks are noticed; one with a systematic $\omega-T$ dispersion, corresponding to the shoulder (feature P2 in Fig. 2(a)) and another, relatively frequency in-deviant one around $\sim 320\text{K}$. The latter peak in $d\varepsilon'/dT$ is close to T_1 , signaling a magneto-electric (ME) coupling. Upon cooling across this temperature, the usual steeply-

decreasing $\varepsilon'_\omega(T)$ (consequent to the increasing polarization \mathbf{P}) give way to the gradually-sloping plateaus (Fig. 3(b)). Emergence of plateaus at ~ 320 K (relatively frequency-indifferent) signifies spin-order imposed breakage of the quasi-long-range polar state— resulting in the response of smaller entities lacking a sizescale, as reckoned below. Furthermore, shoulders near T_2 dispersed across $\sim P_2$ (plateaus’ demise) clearly evidence another magneto-electric switchover, to a reentrant segmental electrical-organization (size-distributed entities’ response), triggered by the second magnetic anomaly. Loss tangent $\tan\delta_\omega(T)$ in Fig. 3(c) shows dispersive peaks, shifting towards higher temperature at increasing frequency. Above ~ 227 K, magnitude and dispersion of $\tan\delta(T)$ change abruptly, as illustrated by the locus of the peak-maxima. Interestingly, this temperature coincides with T_2 . Note that the typical “flat loss” spectral feature [17] is not observed here, which characterizes the relaxor ferroelectrics viz., the merging of loss tangent curves of different frequencies on their lower-temperature side. Therefore, the data apparently rule out the signature of polar nano regions (PNR’s)/relaxor state, consequent to the expected electric-phase-changes at the T_1 and T_2 .

We reiterate that the smeared peaks obtained here in the dielectric constant within close proximity of our designated $T_C \sim 355$ K are not rooted in relaxations, since the associated loss tangent values (inset of Fig. 3(c)) are devoid of any otherwise-necessitated peaks/maxima. Neither do the imaginary-permittivity/modulus and real-impedance functions feature any peaks over the same T -window. Importantly, no generic relaxations in the dielectric spectra accompany a peak feature in the heat capacity data, which we clearly observe near T_C (inset of Fig. 3(a)). Large measured permittivity ($\sim O(10^3)$ near 355K) is commensurate with that of other ferroelectrics’ near their T_C [18], including that of the single crystal KDP [19]. In a very recent review, Scott and Gardner [20] have observed that in typical magneto-electric materials, somewhat ‘imperfect/distorted FE signatures’ often indicate the existence of quasi-local order, which grows into robust/long-range ferroelectricity in their nanostructured/thin-film formations, as confirmed in the case of samarium orthoferrite (SmFeO_3) by Chaturvedi et. al. [21]. Nature of the sub- T_C relaxation kinetics, evaluated below, serves to recognize the exact electrical phases in the hexagonal SBMO, coexistent with its intricate magnetically ordered state(s).

For a precise determination of the electrical relaxation character, fits on the frequency-domain $\tan\delta_I(\omega)$ were performed (Fig. 3(d)), using general Havriliak-Negami (H-N) expression for the complex permittivity [15]:

$$\varepsilon^* = \varepsilon' - i\varepsilon'' = \frac{\Delta\varepsilon}{[1+(i\tau\omega)^\alpha]^\beta} - i\left(\frac{\sigma_0}{\varepsilon\omega}\right)^n + \varepsilon_\infty \quad (1)$$

Where ε^* is the complex permittivity, ε'' is imaginary permittivity, $\Delta\varepsilon$ is known as dielectric strength of the material, τ is the mean relaxation time, σ_0 is d.c. conductivity, and ($0 \leq \alpha, \beta \leq 1$) parameterize the width (broadening) and shape (asymmetry) of relaxation peak spectra, respectively. Optimized $\alpha, \beta \neq 1$ from the H-N fits to $\tan\delta_I(\omega)$ spectra mark their asymmetry (Fig. 3(d)) and T -dependent/extralorentzian FWHM (inset), affirming the non-Debye nature of the observed relaxations [15]. Corroborating the inference drawn from analyzing the room temperature data (Fig. 2), the non-Debye character clearly discounts any significant extrinsic contributions to the dielectric response due, e.g., to the Maxwell-Wagner type inter-granular free charges, or to the hopping of intra-granular oxygen-ions. Such independent and uncorrelated polaronic degrees of freedom represent extraneous and conduction-dominant responses, which may feature generic Lorentzian relaxation at very low frequencies, corresponding to the basic Debye exponential time-decay dynamics [22].

Accurate $\tau(T)$ obtained from the optimum H-N fits is plotted as $\ln(\tau)$ versus T in Fig. 4. Clear change of curvature in $\ln(\tau)-T$ at 220K reveals two types of relaxation mechanisms (I and II). Region II indicating low temperature divergence fits the characteristic power-law for cluster glasses, borrowed from critically-diverging dynamics of spin-glasses [23];

$$\tau = \tau_o \left(\frac{T-T_g}{T_g} \right)^{-z\nu} \quad (2)$$

Here τ_o is the approach time for the nascent (just nucleated) dipole-clusters, T_g is the glass transition temperature, and $z\nu$ is dynamic exponent. Best fit yielding $\tau_o = 10.79\mu\text{s}$, $T_g = 100.83\text{K}$, and $z\nu = 7.39$ is shown in Fig. 4. Optimized dynamic critical exponent is comparable to that for BaTi_{0.65}Zr_{0.35}O₃ (BTZ35) [24], and for the 3D magnetic dipolar glass LiHo_{0.045}Y_{0.955}F₄ [25]. Richert et. al. [26] showed in a calculation that asymmetry ($\beta \neq 1$) of relaxation peak reflects as longer $\tau_{\text{H-N}}$ (by up to $\times 3.6$ here) versus the τ_m read off directly from the peak-maxima— latter

commonly used in Eq. 2. Rising sluggishness $\left(\tau \xrightarrow[T \rightarrow T_g]{} \infty\right)$ of dynamically cooperative glassy clusters owes to their diverging size-scale $\left(\xi \xrightarrow[T \rightarrow T_g]{} |T - T_g|^{-\nu}\right)$, since the critical relaxation time itself scales with the correlation length as $\tau \sim \xi^z$ [27, 28]. Taking $z \approx 3$ for reasonably isotropic (bulk) correlations—comparison with typical relaxor-PNR's (size $\sim O(\text{nm})$ and approach time $\sim O(10^1)$ ps) estimates the cluster size here as $\xi_{\text{SBMO}} \sim O(10^2)$ nm—the mesoscopic scale.

The anomalous/non-activated behavior of $\tau(T)$ in region I (Fig. 4), bending over to saturation on the lower- T side—also witnessed in (Gd, Eu, Tb, Dy)MnO₃ by Schrettle et. al. [29]—indicates local quantum tunneling mechanism [30] for the relaxation dynamics, involving small groups of only a few dipoles, lacking barrier-activation and size (distribution). This explains frequency-independent origin of $\varepsilon'_\omega(T)$ -plateaus, as the response due to nominally-cooperative entities, defining no lengthscale. A generic/polynomial fit to $\ln\tau(T)$ here yields $\tau_{\text{sat}} \approx 4.4\mu\text{s}$ for the asymptotic low- T relaxations over 220-245K, which may relate to the basic quantum tunneling rate. Interestingly, the quantum mechanical tunneling (QMT) is also indicated in this regime by a relatively constant Jonscher power-law index $n(T)$ [30] of our a.c. conductivity isotherms $\sigma_T(\omega) = \sigma_{dc}(T)[1+(\omega\tau)^n]$ (not presented here).

We have directly witnessed the essential aging and rejuvenation attributes of the electrical cluster glass phase (region II in Fig.4) by performing the isothermal waiting experiments below and above T_g . Following the standard protocol similar to as employed e.g., in the literature [31, 32], our results for the dielectric constant measured at 15 Hz over 50-160K are shown in Fig. 5. We chose the low probing frequency, so the bigger magnitudes of both the dielectric constant and the changes in it, measured over the temperature window of interest, provided a good signal to noise ratio for the aging effects as well. We first note that the uninterrupted baseline runs (① & ②) at uniform temperature-ramps ($\pm 0.5\text{K/min}$, solid & dash line curves in the main panel) reveal a clear hysteresis between the cooling and warming data, along with their excellent overlaps at the lower and upper temperature-ends. This anomalous & novel feature is hitherto unreported, to the best of our knowledge, and its reproducivity has been duly verified by us over repeated cycles. Secondly, the isothermal aging/annealing in otherwise uniformly cooled run (③; open stars in the main panel) involved several hours' waiting and data collection each at three temperatures viz., $\sim 1.1T_g$, $0.9T_g$, and $3/4T_g$ (lower inset). Clearly

measurable $\sim O(10)\%$ decays in dielectric constant were recorded in the isothermal experiments. Fractional falls during aging at these selected temperatures below the uniform cooling baseline are shown in the upper inset. Asymptotic rejuvenations back to the uniform cooling baseline (to within $\sim 2\%$) in the post-isothermal/succeeding cooling laps are similar to those reported for the electrical cluster glasses [33] and for spin glasses [34]. Also shown in main panel is the uniformly warm up data (④; open circles in the main panel) taken immediately after the cooling run interrupted with the three isothermal waitings. Surprisingly, in this special warm up run, we did not encounter any detectable trace of the dielectric ‘holes’ created at the isothermal waiting temperatures. This anomalous absence of the so-called ‘memory’ effect has been reproducibly confirmed over repeated such cycles. The excellent overlap of post-aging (circles) and generic (dashes) warm up runs’ data, over the full temperature range of observation is remarkable. We did not find a repeat cooling run ⑤ measurably different from the original baseline uniform cooling ①, and the same is not shown here for clarity. Essentially, all the same features, albeit having rather low signal-to-noise ratios, were also observed at 110 Hz probing frequency.

Consistent with sub- T_g non-ergodicity (inability of glassy state to visit all its dynamically sluggish metastable states on finite timescale), relatively largest (upper inset) & slowest (lower inset) isothermal-aging-drop in ε' are seen during waiting at 91K (i.e., just below T_g). Consolidation of dynamical freezing with further lowering of temperature (with still possible thermal activation of yet-fewer/incompletely-frozen/less-sluggish metastable states) causes a lower drop at $\sim 3/4T_g$. We are given to understand the ‘no memory’ (warm up run, ④) signals witnessed here as consistent with fairly large and fast isothermal aging attribute— decays completed at the waiting temperatures within $\sim O(\text{hr})$ (lower inset, also see [32]), along with the rapid rejuvenations on reverting back to the cooling lapses of the run ③. As per discussed in the next sections, witnessed increase & decrease of the Mn-O bonds’ inequivalence and phonon softening & hardening— signifying high flexibility of the local structural adjustments and vibronic attributes— are the definitive convict for the observed features of our aging/rejuvenation/memory findings.

Temperature dependent XRD patterns (150K-350K) were recorded using synchrotron source. $R_{\text{exp}} = 9.14\%$, $R_{\text{wp}} = 11.4\%$, $R_p = 10.4\%$, $\chi^2 = 1.56$ were obtained for 300K, giving a respectable fit [35]. XRD patterns upto lowest temperature measured reveal that the crystal

symmetry remains P6₃/mmc down to low temperatures, thereby ruling out a robust (long range) ferroelectric ordering. In Fig. 6(a) we have plotted the difference in Mn-O and Mn-O1 bond lengths (Δ) versus temperature. At 350K, we observe inequivalent Mn-O and Mn-O1 bond lengths. Here, in MnO₆ octahedra, bond length between Mn-O1 and Mn-O differs by $\sim 0.05\text{\AA}$ (inset of Fig. 6(a)). Therefore, inversion symmetry is locally broken in SBMO, which is the driving factor for the observed ferroelectricity at $\sim 355\text{K}$, although SBMO maintains overall centrosymmetric P6₃/mmc structure over the studied temperature range. Local nature of the inversion symmetry-breaking is but reflected as the $\pm 3\text{K}$ spread obtained in the FE- T_C , vs. the probing frequency (Fig. 3(a)). It should be noted that though Rietveld analysis provides information related to an average long-range structure, yet at local or short range level, the structure can adopt non-centrosymmetric character, yielding inequivalent bond lengths [36-41]. Furthermore, numerical calculations have shown that the local breaking of inversion symmetry directly controls the microscopic origin of the Boson peak in model crystal systems [42]. It is also observed from Fig. 6(a) that Δ increases with decrease in temperature down to $\sim 330\text{K}$, reflecting the enhancement of local inversion symmetry breaking. We denote 330K-350K as the ferroelectric region (FR).

As is evident from Fig. 3(b), a plateau behavior in the dielectric constant emerges below T_1 ; reflected as ‘frequency in-deviant’ peaks in $d\epsilon'/dT$ near 320K (inset). From Fig. 6(b), which shows the shift in Mn position along z -direction, it is evident that below T_1 , antiferromagnetic exchange J_1 significantly z -shifts the Mn-atoms. The shift Δz of Mn causes an ‘ambivalent drop’ in Δ , which suppresses/stagnates the polarization. These observations suggest that here the dominant magnetic interaction ($J_1 \gg J_2$) opposes the local inversion symmetry breaking. Hence, below T_1 , effective magnetic exchange energy clearly works against the elasto-electric interaction energy. We denote this temperature range (325K-227K) as the tunneling region (TR).

With further decrease in temperature below T_2 , Mn shifts in the opposite z -direction, (Fig. 6(b)). This Δz turnover of Mn-position reflects the rise-back of bond-length inequivalence (co-increasing Δ , (Fig. 6(a)), leading to a ‘reentrant buildup’ of dynamic dipolar correlations. The magnetic anomalies at T_1 and T_2 combined with the associated spin-phonon coupling cause zig-zag variation of $\Delta(T)$ across the TR regime, leading to cooperatively relaxing dipoles with sluggish/glassy character (up to only meso-sized, $\sim O(10^2)$ nm) upon cooling. We denote the

temperature range below 225K as the glass region (GR). Shifts in the Mn z -position also lead to concurrent variations in the Mn-O-Mn bond-angle (Fig. 6(c)), which too reflects anomalies across T_1 and T_2 . Singh et. al. showed for 0.9BiFeO₃-0.1BaTiO₃ composite that while the structure remains the same, change in bond-angle across the magnetic transition temperature and hence, shifts in the position of atoms attributes to the origin of ferroelectricity [43].

The observed magneto-structural-vibrational coupling is further manifest in the Mn-displacement E_{1g} Raman mode, as shown in inset of Fig. 6(c). Across the ferroelectric transition (T_C) and magnetic anomalies (T_1 and T_2), mode-position deviates from the usual thermal anharmonic background. Below T_C , softening of the phonon mode is expected. Therefore, due to the competition between ferroelectricity build-up and anharmonic behavior, a fleeting ‘stagnation’ of Raman shift is observed just below T_C . The re-softening trend below 250K itself suggests that precursor effects of the second antiferromagnetic (non-linear Mn-O-Mn superexchange) interaction are present in the system even above $T_2 = 227$ K. These findings evidence that the exchange interactions cause anomalies in the lattice vibrations across T_i -values, confirming the spin-phonon coupling in SBMO [12, 44, 45], also observed in strained EuTiO₃, cubic SrMnO₃, and Ba-doped cubic SrMnO₃ multiferroics— through softening of their magnetic-ion related phonon mode—as a crucial signature for multiferroicity [7, 8, 46].

Now we discuss the rationale for the observed magnetic behavior. In SBMO, an intricate magnetic behavior is anticipated. The unit cell (*u.c.*) of this 4H structure has two face-sharing Mn₂O₉ bi-octahedra; which in turn link together in a corner-sharing fashion through a common oxygen (Fig. 7(a)). The corner-shared linkage leads to a 180° antiferromagnetic superexchange (AF-SE) (J_1) in the network. Further, within the bi-octahedra, the short Mn⁴⁺-Mn⁴⁺ distances (~2.50 Å) and the ~80° Mn⁴⁺-O-Mn⁴⁺ triads through the face-shared oxygen atoms lead to direct- (J_D) and super-exchange (J_S) interactions respectively, giving rise to an effective magnetic exchange J_2 . The actual strength and sign of the magnetic interactions J_1 and J_2 will depend on the extent of the orbital overlap between the magnetic ion and the intervening oxygen [47]. Convolution of the microscopic exchange interactions at work over particulate temperature windows effectively determines the magnetization status of the system therein.

From our magnetic data, as shown in Fig. 7(b) we observe that below 325 K, the magnetization starts decreasing gradually; albeit the width of the transition is rather broad.

Below 225 K however, magnetization drops even more gradually, with a discontinuity in its slope. Though our temperature dependent XRD experiments show no significant change in the *u.c.* dimensions around this temperature, the Mn_z position and Mn-O-Mn bond angles show clear anomalies. We notice that the Mn-O1-Mn linkages corresponding to the 180° superexchange interactions through the corner-linking oxygen show a gradual changeover in bond distances close to 325 K; though the magnitude of the change is relatively small, the bond angle remains almost linear throughout the temperature range studied here. On the other hand, the Mn-O-Mn bonds within the bi-octahedra undergo a sharp variation close to 225 K; the Mn-O-Mn bond lengths change by about 0.1 Å (~2.5%), and angles show an overall $\sim 1^\circ$ change.

The structural information presented above suggests that sharp changes in the magnetic exchange interactions are plausible close to 225 K. These are further corroborated with anomalies in the E_{1g} mode-position, observed in the temperature dependent Raman spectra. Thus, the magnetic anomaly occurring at 225 K can be associated with local structural changes, implying spin-phonon coupling. An electronic model that incorporates spin-spin, phonon-phonon, and spin-phonon interactions is necessary to describe such mechanisms. This is further complicated by the spin-orbit interactions of the metal ion and the crystal field effects due to the surrounding ligands in the octahedron. The Heisenberg spin-Hamiltonian, being a mean-field model, does not describe such interactions adequately. However, a rudimentary way to model this is by fitting the magnetization data, using an effective spin-Hamiltonian for the two temperature regimes namely; (1) $T > 225$ K, wherein antiferromagnetic interaction between Mn^{4+} ions of linear Mn-O1-Mn bonds leads to short range correlations (SRC) and, together with weak interactions between Mn^{4+} ions of non-linear Mn-O-Mn bonds, give rise to a broad feature at 325 K, and (2) $T < 225$ K, where the local structural changes sharply increase the intra-bioctahedral Mn-O-Mn antiferromagnetic interactions, resulting in long-range correlations (LRC).

The magnetic data can be modeled by considering the Hamiltonian,

$$\hat{H} = -\hat{J}_1 \hat{S}_2 \cdot \hat{S}_3 - \hat{J}_1 \hat{S}_4 \cdot \hat{S}_1 - \hat{J}_2 \hat{S}_1 \cdot \hat{S}_2 - \hat{J}_2 \hat{S}_3 \cdot \hat{S}_4 \quad (1)$$

With $J_2 \ll J_1$ for $T > 225$ K and $J_2 \gg J_1$ for $T < 225$ K, where, J_1 (J_2) corresponds to the strength of inter (intra) -bioctahedral exchange interaction, S_i 's are the spin operators, and the subscripts on the spin operators correspond to the indices of Mn^{4+} sites in a *u.c.* The interaction between sites ‘4’ and ‘1’ imposes the periodic boundary condition in the *u.c.* Positive (negative)

values of J_i correspond to ferromagnetic (antiferromagnetic) interactions. The model Hamiltonian in eq.(1) conserves both total \hat{S}^2 and \hat{S}_Z operators and hence it is possible to construct the Hamiltonian matrix (H) either in total- S or in total- M_S basis. However, in this case the H -matrix is constructed in constant- M_S basis, and then the eigenstates $E(S, M_S)$ of the spin model are numerically obtained by full diagonalization [48]. The expectation values of the \hat{S}^2 and \hat{S}_Z operators for each eigenstate are obtained, from which the total spin S and M_S of the state are deduced. Finally, the magnetization of the system as a function of temperature (T) at a chosen magnetic field (H_z) is obtained from the relation,

$$M(H, T) = N_A g \mu_B \frac{\sum_S \sum_{M_S} M_S e^{-\frac{[E(S, M_S) - g\mu_B H_z M_S]}{k_B T}}}{\sum_S \sum_{M_S} e^{-\frac{[E(S, M_S) - g\mu_B H_z M_S]}{k_B T}}} \quad (2)$$

where, N_A is the Avogadro number, μ_B is the Bohr magneton value, g is the Lande g -factor (taken to be 2.0), and magnetic field H_z is set to 0.01 Tesla, as per the experiments. The magnetic data in the temperature range 225K-350K is fitted by iterating over the values of J_1 and J_2 (Figure 7(b)). Our best fit for the magnetization data in this temperature region yields $J_1 = -18$ meV and $J_2 = -2.16$ meV. We further notice that the value of magnetization for the highest temperature reported is far less than the spin-only moments of four uncorrelated spin-3/2 species per *u.c.* i.e., 3.3×10^{-3} emu/gm; suggesting that even at 350 K, the system has not transformed fully into the paramagnetic state. In order to understand this, we computed the energy spectrum of spin- 1/2, 1, and 3/2 systems using the above Hamiltonian (Fig 7(c)), keeping the values of the model parameters unchanged. We notice that, unlike the systems with small site-spins, the spread in the energy of the eigenstates is fairly large for higher site-spins. In order to realize paramagnetic state, it is necessary that all the spin states are populated. However, in our present case, the higher site-spins of Mn⁴⁺ ions lead to states that have wider spread in energy, thus requiring higher temperatures (vis-à-vis J_i/k_B) to reach the paramagnetic state, as confirmed from our magnetic measurements, which did not show any signature of Curie-Weiss behaviour until 750K.

Now, we turn our focus on regime-2, corresponding to temperature values below 225K. Here, we consider the enhanced non-linear Mn-O-Mn superexchange via the face-shared oxygen

plus the direct Mn⁴⁺-Mn⁴⁺ exchange ($J_2 \gg J_1$), that facilitates long-range ordering in the system. This is supported by temperature dependent neutron diffraction studies on similar systems [13], which showed long-range AFM ordering of both intra- and inter-bioctahedral Mn⁴⁺ spins below 270 K. The Hamiltonian (1) is once again solved by the method discussed above, with J_1 fixed at -18 meV. The magnetic data is fitted via iterative process, by allowing only J_2 to vary, with the condition that $J_2 \gg J_1$; our best fit yields $J_2 = -86$ meV. The strong antiferromagnetic nature of the effective interaction J_2 vis-à-vis J_1 can be understood in terms of the contributions from both (enhanced) super- and direct- exchange mechanisms between the Mn⁴⁺ ions within each bi-octahedron.

It should be noted that previous first-principles calculations based on the density functional theory had shown that there is no significant direct overlap of charge densities between the two Mn⁴⁺ ions of the bi-octahedron [49]. However, it should be noted that these calculations were based on ground state structures, and hence the local distortions taking place versus temperature were not taken into consideration. In a related previous study on magnetic properties of 4H-SBMO, the SRC's at high temperatures were assigned to antiferromagnetic fluctuations within the bi-octahedron, and the low temperature properties were described based on the onset of LRC's due to the inter bi-octahedral interactions [50]. On the contrary, our experimental results on the crystal structure, Raman spectra, and magnetic measurements, supported by our theoretical model, show that the broad hump occurring at 325 K is a result of antiferromagnetic fluctuations between Mn⁴⁺ ions of two *adjacent* bi-octahedra, and the long range ordering sets with the sudden increase of magnetic exchange *within* the bi-octahedron, as a result of the local structural distortion.

To further confirm that below 225 K, a different magnetic arrangement takes over, we performed magnetization versus field measurements from 200 K to 300 K at 5 K interval. From these measurements, we plotted the slope of $M-H$ curves versus temperature (Fig. 7(d)), which show an anomaly at 225 K. Thus, our experimental results and model calculations throw light on the strength of the magnetic exchange mechanisms involved in SBMO. Neutron diffraction experiments as well as a microscopic electronic model that includes electron-phonon interactions should deepen our understanding of the complex magnetism in this system, which needs to be further explored.

Magneto-dielectricity MD(%) is given by [51]

$$\frac{\varepsilon'(H) - \varepsilon'(0)}{\varepsilon'(0)} \times 100$$

We measured MD(H) under magnetic field up to 9T at 210K/1kHz and at 300K/1MHz, shown in Fig. 8(a, b). While the isotherm MD_{300K}(H) is all-positive, MD_{210K}(H) is all-negative valued. To discern if and how the (magneto) conductance influences our results, we have also plotted the magneto-loss [51] $\{ML(\%) = \frac{\tan\delta(H)-\tan\delta(0)}{\tan\delta(0)} \times 100\}$ at both 210K (LT) and 300K (RT) in Fig. 8(a, b). Linear MD(H) and low-lying/flat ML(H) (solid lines) yielding |MD/ML|_{LT} ~ +(6-11)dB and |MD/ML|_{RT} ~ +(10-13)dB unambiguously ascertain robust and genuine magneto-dielectricity over ~2-5 Tesla field-window. Moreover, under (5-7)T field, the same order of magnitude changes in MD_{RT} and ML_{RT} (traceable to $\tan\delta \propto (\varepsilon')^{-1}$, by definition) while |MD/ML|_{RT} ≥ +3.5dB evidence little influence yet of room temperature magneto-resistance [51]. Lastly, above ~7T, decreasing MD_{RT} and increasing ML_{RT} of comparable magnitudes are predominantly determined by the (magneto) conductance; thereby rendering the room temperature ME character rather conspicuous at higher fields. The circumstance above ~5T field is evidently more favorable at lower T 's, with suppressed (magneto) conductance; so that |MD/ML|_{LT} ≈ $O(10)$.

To better understand MD_T(H), we performed close by magnetization measurements. From Table 1, it is clear that T_1 and T_2 are both maximum at ~5-6T, above which they both show measurable decreases. Now, referred to Fig. 3(b), T_1 and T_2 respectively mark the sharp start and dispersive demise of the $\varepsilon'(T)$ -plateaus. Therefore, vis-à-vis the usual (otherwise expected) steep decrease of the dielectric constant below T_C , the interjecting 180°-AFM anomaly at T_1 effectively ‘increases’ the ε' -values, while relative to the $\varepsilon'(T)$ -plateaus, the second AFM anomaly at T_2 effectively ‘decreases’ the same. Since the applied field initially increases both T_1 and T_2 , this explains *both* why MD(H) at 300K (below $T_1 = 325$ K) is positive (higher plateau under the field) and at 210K (below $T_2 = 227$ K) is negative (plateau-shoulder occurs at higher temperature under the field). Further, concurring decreases of T_1 and T_2 for $H > 5$ -6T explains the respective turn-backs of MD(H) across ~7T at both 300K and 210K. We finally remark that genuine ME as demonstrated— along with the observed non-Debye relaxation and bulk-nature of the high-frequency response at sub-ambient temperatures— adequately guarantee the ME-origin from an essentially intrinsic dielectric response.

Summarizing our work, it is established that the improper-ferroelectricity manifest in Sr_{0.6}Ba_{0.4}MnO₃ arises from the structure-conserving/locally-unequal Mn-O bond lengths in the MnO₆ octahedra. The magneto-electricity here is due to the Mn-displacement soft-phonon mode being coupled to the spins in the material. The two magnetic anomalies at 325K and 225K here accompany concurrent anomalies in its structural parameters and changes of its electrical states. The smooth magnetization-maximum at 325 K is a result of antiferromagnetic short range correlations between Mn⁴⁺ ions of two adjacent bi-octahedra and owes to the local structural distortion, as per confirmed from calculations with a model spin-Hamiltonian. The long range ordering sets in upon the sudden increase of magnetic exchange interaction between Mn⁴⁺ ions within the bi-octahedron; responsible for the second magnetic anomaly and its associated magneto-electric manifestation. The two particulate magneto-electric effects of opposite signs are traceable to spin-exchange/local-strain frustration for free energy minimization. Here, the crossover upon cooling from the soft-mode ferroelectricity breaking into reentrant cluster-glass phase via tunneling state has been maidenly recognized. The electrical cluster glass phase is well confirmed by its characteristic aging and rejuvenation features. From our study, SBMO comes across as one of the rare multifunctional materials, where FE and AFM orderings occur within a narrow ambient window close to room temperature. In this perspective it is vital to explore the oriented epitaxial films of similar materials, which in bulk form exhibit soft mode FE ordering, even though their global structure is centrosymmetric. Indeed, the observed AFM ordering can also be tuned in such epitaxial films to be ferromagnetic [7], upon choosing a proper epitaxial strain.

Acknowledgements: Authors are thankful to Dr. N.P. Lalla and Ms. Poonam Yadav of UGC-DAE CSR, Indore, for providing zero-field dielectric data. Authors are also thankful to Mr. Anupam Jana and Mr. Gyanendra Panchal for help in recording EDAX and XAS spectra respectively.

References:

- [1] Daniel Khomskii, Physics **2**, 20 (2009).
- [2] Nicola A. Hill, J. Phys. Chem. B **104**, 6694 (2000).
- [3] W. Eerenstein, N.D. Mathur, and J.F. Scott, Nature **442**, 759 (2006).
- [4] Sang-Wook Cheong and Maxim Mostovoy, Nat. Mater. **6**, 13 (2007).
- [5] Daniel K. Pratt Jeffrey W. Lynn, James Mais, Omar Chmaissem, Dennis E. Brown Stanislaw Kolesnik, and Bogdan Dabrowski, Phys. Rev. B **90**, 140401(R) (2014).
- [6] H. Sakai, J. Fujioka, T. Fukuda, D. Okuyama, D. Hashizume, F. Kagawa, H. Nakao, Y. Murakami, T. Arima, A.Q.R. Baron, Y. Taguchi, and Y. Tokura, Phys. Rev. Lett **107**, 137601 (2011).
- [7] Craig J. Fennie and Karin M. Rabe, Phys. Rev. Lett. **97**, 267602 (2006)
- [8] S. Kamba, V. Goian, V. Skoromets, J. Hejtm' anek, V. Bovtun, M. Kempa, F. Borodavka, P. Van'ek, A.A. Belik, J.H. Lee, O. Pacherov'a, and K.M. Rabe, Phys. Rev. B **89**, 064308 (2014).
- [9] H.J. Xiang, Su-Huai Wei, M.-H. Whangbo, and Juarez L.F. Da Silva, Phys. Rev. Lett. **101**, 037209 (2008).
- [10] A. Malashevich and D. Vanderbilt, Phys. Rev. Lett. **101**, 037210 (2008).
- [11] W. Kleemann, S. Bedanta, P. Borisov, V.V. Shvartsman, S. Miga, J. Dec, A. Tkach and P.M. Vilarinho: Eur. Phys. B **71**, 407 (2009).
- [12] Ritu Rawat, D.M. Phase, and R.J. Choudhary, J. Magn. Magn. Mater. **441**, 398 (2017).
- [13] A. Daoud-Aladine, C. Martin,, L.C. Chapon, M. Hervieu, K.S. Knight, M. Brunelli, and P.G. Radaelli, Phys. Rev. B **75**, 104417 (2007).
- [14] P. Lunkenheimer, V. Bobnar, A.V. Pronin, A.I. Ritus, A.A. Volkov, and A. Loidl, Phys. Rev. B **66**, 052105 (2002).
- [15] *Broadband Dielectric Spectroscopy*, edited by F. Kremer and A. Schönhals (Springer, Berlin, 2002).
- [16] *Impedance Spectroscopy Theory, Experiment, and Applications* (2nd ed.), edited by E. Barsoukov and J.R. Macdonald (John Wiley and Sons, New Jersey, 2005), pp295-296.
- [17] V.V. Shvartsman, J. Zhai, and W. Kleemann, Ferroelectrics **379**, 77 (2009).
- [18] *Physics of Ferroelectrics: A modern perspective*, edited by Karin M. Rabe, Charles H. Ahn, and Jean-Marc Triscone (Springer, 2007).
- [19] Jitender Kumar and A.M. Awasthi, Appl. Phys. Lett. **103**, 132903 (2013).

- [20] J.F. Scott and J. Gardner, (2018), <https://doi.org/10.1016/j.mattod.2017.12.003>.
- [21] Smita Chaturvedi, Priyank Shyam, Rabindranath Bag, Mandar M. Shirolkar, Jitender Kumar, Harleen Kaur, Surjeet Singh, A.M. Awasthi, and Sulabha Kulkarni, Phys. Rev. B **96**, 024434 (2017).
- [22] Wei Li and Robert W. Schwartz, Phys. Rev. B **75**, 012104 (2007).
- [23] P.C. Hohenberg and B.I. Halperin, Rev. Mod. Phys. **49**, 435 (1977).
- [24] W. Kleemann, S. Miga, J. Dec, and J. Zhai, Applied Physics Letters **102**, 232907 (2013).
- [25] J.A. Quilliam, S. Meng, C.G.A. Mugford, and J.B. Kycia, Phys. Rev. Lett. **101**, 187204 (2008).
- [26] R. Richert, F. Stickel, R.S. Fee, and M. Maroncelli, Chem. Phys. Lett. **229**, 302 (1994).
- [27] D.S. Fisher, Phys. Rev. Lett. **56**, 416 (1986).
- [28] E.W. Fischer, E. Donth, and W. Steffen, Phys. Rev. Lett. **68**, 2344 (1992).
- [29] F. Schrettle, P. Lunkenheimer, J. Hemberger, V. Yu. Ivanov, A.A. Mukhin, A.M. Balbashov, and A. Loidl. Phys. Rev. Lett. **102**, 207208 (2009).
- [30] S.R. Elliott, Advances In Physics **36** (2), 135 (1987).
- [31] V.V. Shvartsman, S. Bedanta, P. Borisov, W. Kleemann, A. Tkach, and P.M. Vilarinho: Phys. Rev. Lett. **101**, 165704 (2008).
- [32] S.S.N. Bharadwaja, J.R. Kim, H. Ogihara, L.E. Cross, S. Trolier-McKinstry, and C.A. Randall, Phys. Rev. B **83**, 024106 (2011).
- [33] W. Kleemann, J. Dec, and S. Miga, Phase Transitions **88**(3), 234 (2015).
- [34] P.E. Jönsson, Adv. Chem. Phys. **128**, 191 (2004).
- [35] B.F. Toby, Powder Diffr. **21**, 67 (2006).
- [36] Tathamay Basu, V.V. Ravi Kishore, Smita Gohil, Kiran Singh, N. Mohapatra, S. Bhattacharjee, Babu Gonde, N.P. Lalla, Priya Mahadevan, Shankar Ghosh, and E.V. Sampathkumaran, Scientific Reports **4**, 5636 (2014).
- [37] Claudy Rayan Serrao, Asish K. Kundu, S.B. Krupanidhi, Umesh V. Waghmare, and C.N.R. Rao, Phys. Rev. B **72**, 220101(R) (2005).
- [38] K. Ramesha, A. Llobet, Th. Proffen, C.R. Serrao, and C.N.R. Rao, J. Phys.: Condens. Matter **19**, 102202 (2007).
- [39] M. El Amrani, M. Zaghrouri, V. TaPhuoc, F. Gervais, and Néstor E. Massa, J. Magn. Magn. Mater. **361**, 1-6 (2014).

- [40] T.A. Tyson, T. Wu, K.H. Ahn, S.-B. Kim, and S.-W. Cheong, Phys. Rev. B **81**, 054101 (2010).
- [41] Sina Hashemizadeh, Alberto Biancoli, and Dragan Damjanovic, J. Appl. Phys. **119**, 094105 (2016).
- [42] R. Milkus and A. Zacccone, Phys. Rev. B **93**, 094204 (2016).
- [43] Anar Singh, Vibhav Pandey, R.K. Kotnala, and Dhananjai Pandey, Phys. Rev. Lett. **101**, 247602 (2008).
- [44] S. Kamba, D. Nuzhnny, M. Savinov, J. Šebek, and J. Petzelt, Phys. Rev. B **75**, 024403 (2007).
- [45] R. Gupta, G. Venkateswara Pai, A.K. Sood, T.V. Ramakrishnan, and C.N.R. Rao, Europhys. Lett. **58** (5), 778 (2002).
- [46] V. Goian, F. Kadlec, C. Kadlec, B. Dabrowski, S. Kolesnik, O. Chmaissem, D. Nuzhnny, M. Kempa, V. Bovtun, M. Savinov, J. Hejtmánek, J. Prokleška, and S. Kamba, J. Phys.: Condens. Matter **28**, 175901 (2016).
- [47] Rajamani Raghunathan, Jean-Pascal Sutter, Laurent Ducasse, Cédric Desplanches, and S. Ramasesha, Phys. Rev. B **73**, 104438 (2006).
- [48] S. Sahoo, R. Raghunathan, S. Ramasesha, and D. Sen, Phys. Rev. B **78**, 054408 (2008).
- [49] Rune Søndenå, P. Ravindran, and Svein Stølen, Phys. Rev. B, Vol **74**, 144102 (2006).
- [50] P.D. Battle, T.C. Gibb and C.W. Jones, J. Sol. State Chem., Vol **74**, 60 (1988)
- [51] Suchita Pandey, Jitender Kumar, and A.M. Awasthi, J. Phys. D: Appl. Phys. **47**, 435303 (2014).

Figure Captions:

Fig.1 (a) XRD pattern using lab source fitted with Rietveld refinement and Le-bail fitting confirming P6₃/mmc symmetry. (b) EDAX spectra of SBMO sample showing the elemental composition in the sample. (c) Near edge X-ra absorption spectra at Mn L-edge of SBMO and reference MnO₂ sample. (d) Arrangement of atoms for P6₃/mmc symmetry in xz plane drawn using Vesta software (Note: two sites of oxygen-- O and O1 and J₁ and J₂ interaction).

Fig. 2 Nyquist plot of complex impedance at room temperature clearly delineates the extrinsic (electrode surface layer and grain-boundary) responses at low frequency as showing linear Z'' vs. Z' regimes (right inset, with concurrent ‘constant’ phase angle shown in the left inset/left y-axis) and almost flat $\sigma(\omega_{lo})$ ’s (left inset, right y-axis), confined below $\sim 1\text{kHz}$. On the other hand, higher frequency $Z''(Z')$ semicircular arc and Jonscher power-law fitted $\sigma(\omega_{hi})$ (with $\sigma_{dc}^g < \sigma_{dc}^{tot}$) both manifest the dominant bulk/grain contribution. The extrinsic/intrinsic crossover frequency ($\omega_{co}^{300\text{K}} \sim 1\text{kHz}$) shifts to lower values upon cooling.

Fig. 3 (a) Dielectric constant $\epsilon'(T)$ at selected frequencies (P1 indicates the ‘dispersion-free’ FE- T_C and P2 marks the glassy-dispersion). Inset shows the associated C_p -peak near T_C , (b) $\epsilon'(T)$ on log-log plot reveals the plateau region while $d\epsilon'/dT$ in the inset indicates the dispersive ϵ' -knee temperature-window and the benchmark start of ϵ' -plateaus (arrows indicate increasing frequency), (c) $\tan\delta(T)$ at different frequencies with the peak-height profile showing abrupt rise above $\sim T_2$. Inset shows a featureless (‘no-peaks’) behaviour near the FE- T_C ; clearly ruling out a relaxational origin of the non-sharp peaks at the temperature in Fig. 3(a)), and (d) $\tan\delta(\omega)$ at several temperatures (solid lines are H-N fits), inset shows the peaks’ full width at half maximum FWHM(T).

Fig. 4 $\ln(\tau)$ versus T ; solid line fit in region II illustrates glassy behaviour while the inset shows $\ln(\tau)$ versus $\ln(T/T_g - 1)$, with solid straight line as the fit.

Fig. 5 Aging measurements of dielectric constant at 15Hz frequency and $\pm 0.5\text{K}/\text{min}$ temp-ramp rate under the following protocol— ① baseline uniform cooling (solid curve), ② baseline uniform warming (dashed curve), ③ uniform cooling intercepted by isothermal waiting/annealing at $T_w = 1.1T_g$, $0.9T_g$, and $3/4T_g$ (open stars), and ④ uniform warming immediately post the cooling/aging run (open circles). Upper inset— fractional drops in

permittivity at the annealed temperatures and its rejuvenation back towards the baseline-cooling values, during the sectional cooling lapses after the isothermal annealing. Lower inset—exponentially-decaying time profiles of ε'_{T_w} -drops at the annealing temperatures T_w , over the isothermal waiting times $t_w \sim O(\text{Hrs})$.

Fig. 6 (a) Difference between Mn-O1 and Mn-O bond length (Δ) plotted versus Temperature (solid line is guide for eyes), inset shows MnO_6 octahedra, (b) shift in Wyckoff position of Mn along z -direction with respect to temperature and (c) shows change in bond angle Mn-O-Mn versus temperature. Inset in (c) shows Raman shift of E_{1g} mode plotted with respect to temperature (T) which reveals shift from anharmonic behavior (shown by O symbol).

Fig.7 (a) Schematic of the magnetic model, showing the pathways of magnetic exchange and the corresponding exchange strengths in LRC and SRC regimes. (b) Magnetization vs. temperature fits (continuous lines) of SBMO in SRC and LRC regimes. The experimental values are shown as red circles. The magnetization curve computed in either of these two regimes is extended into the other, to emphasize the change in slope across the magnetic anomaly. (c) Eigen spectrum of the spin model for 4-site spin-1/2, 1, and 3/2 systems for the Hamiltonian in eq. 1. (d) Slope of the $M-H$ curves recorded at different temperatures across T_2 , dashed line is guide to the eye.

Fig. 8 Magneto-dielectricity (MD) and magneto-losses (ML) versus the applied field H at (a) 1kHz/210K, and (b) at 1MHz/300K, with behavior changes at benchmarked applied fields.

Table-I: Variation of T_1 and T_2 with magnetic field.

Table-I. Variation of magnetic-anomalies temperatures (T_1 and T_2) with applied \mathbf{H} -field.

Magnetic Field (Tesla)	T_1 (K)	T_2 (K)
0.01	325	227
5	336.5	267
6	337.5	265
7	315	250

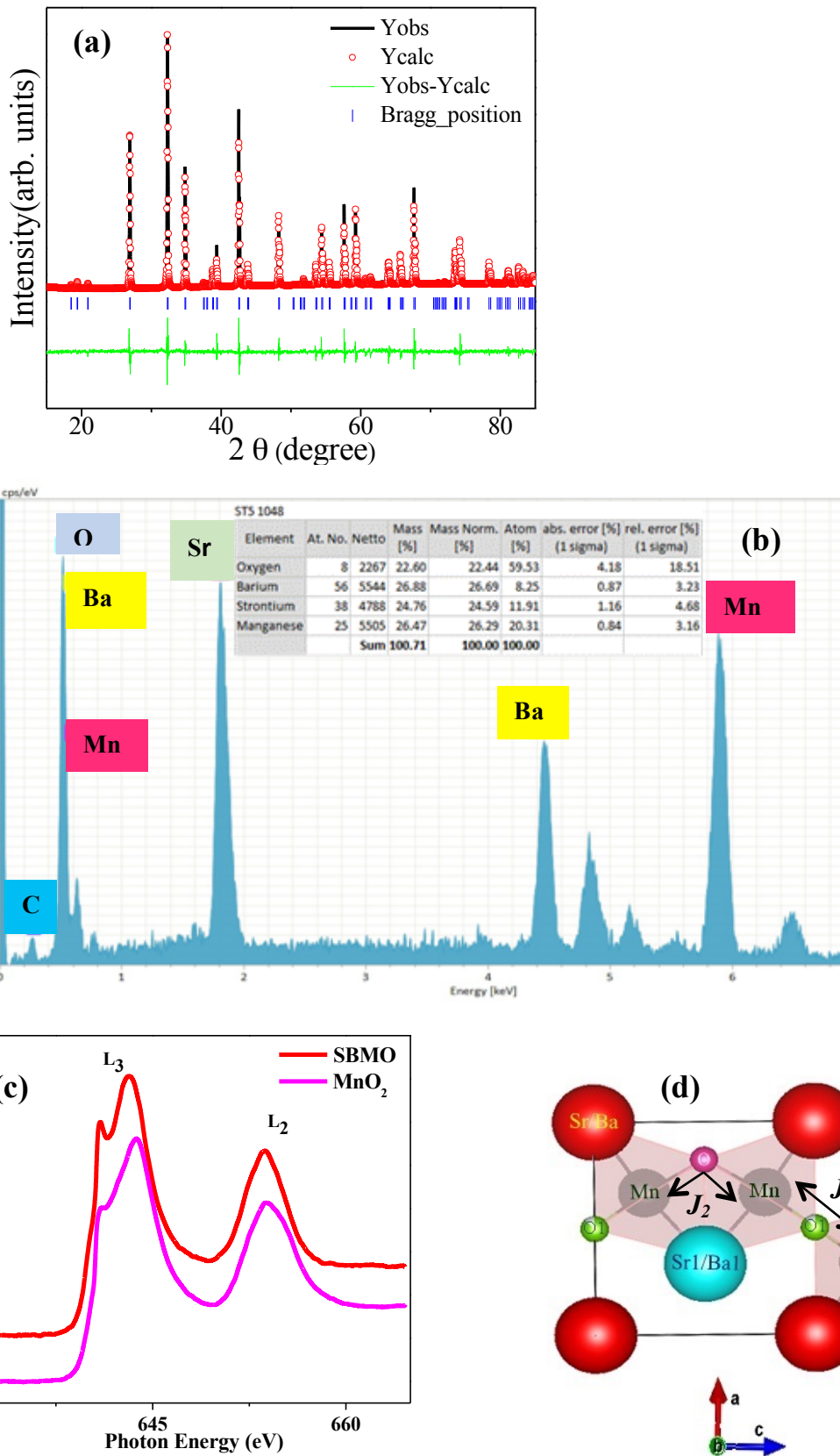


Fig. 1

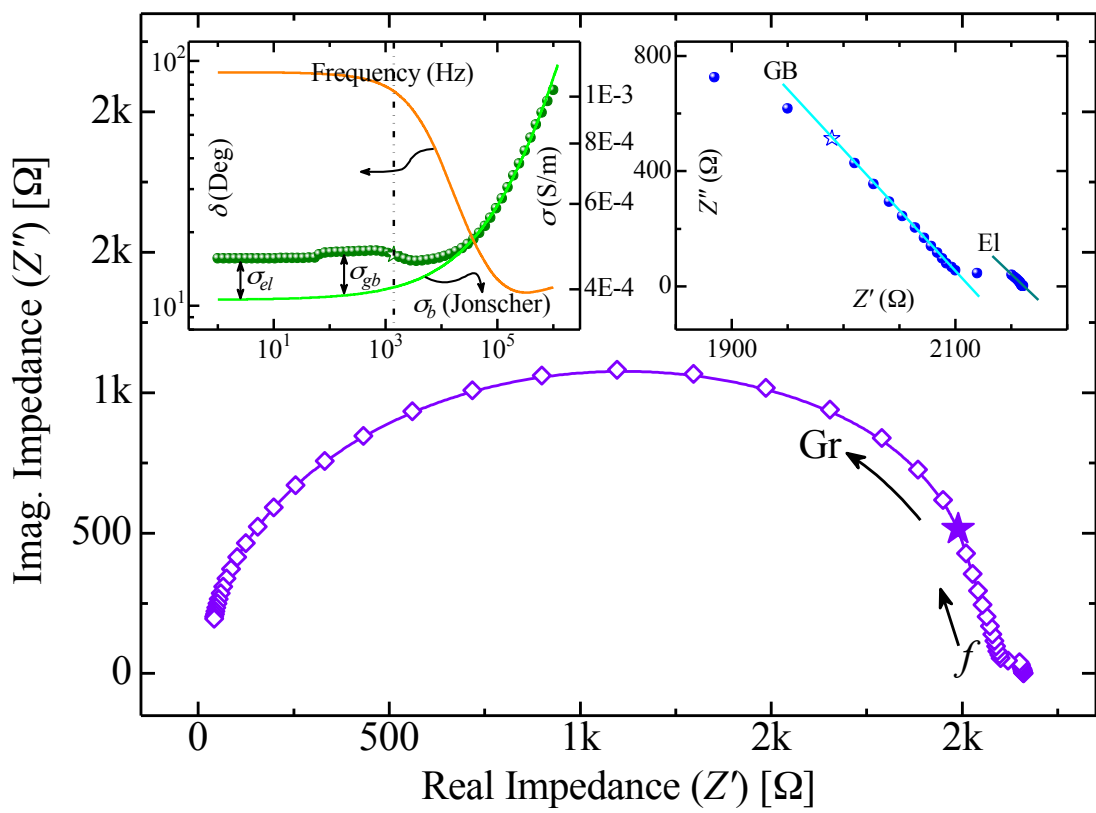


Fig. 2

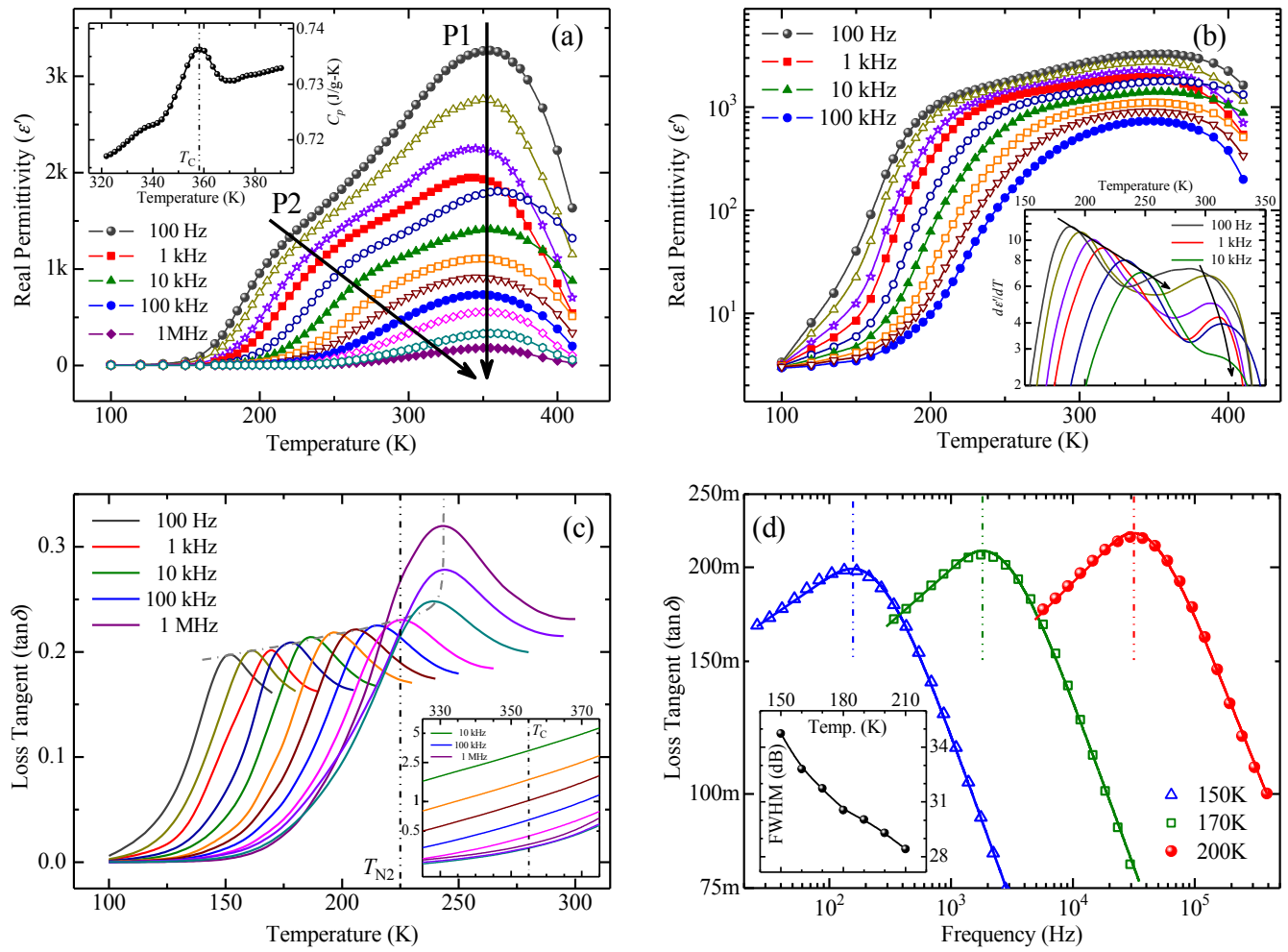
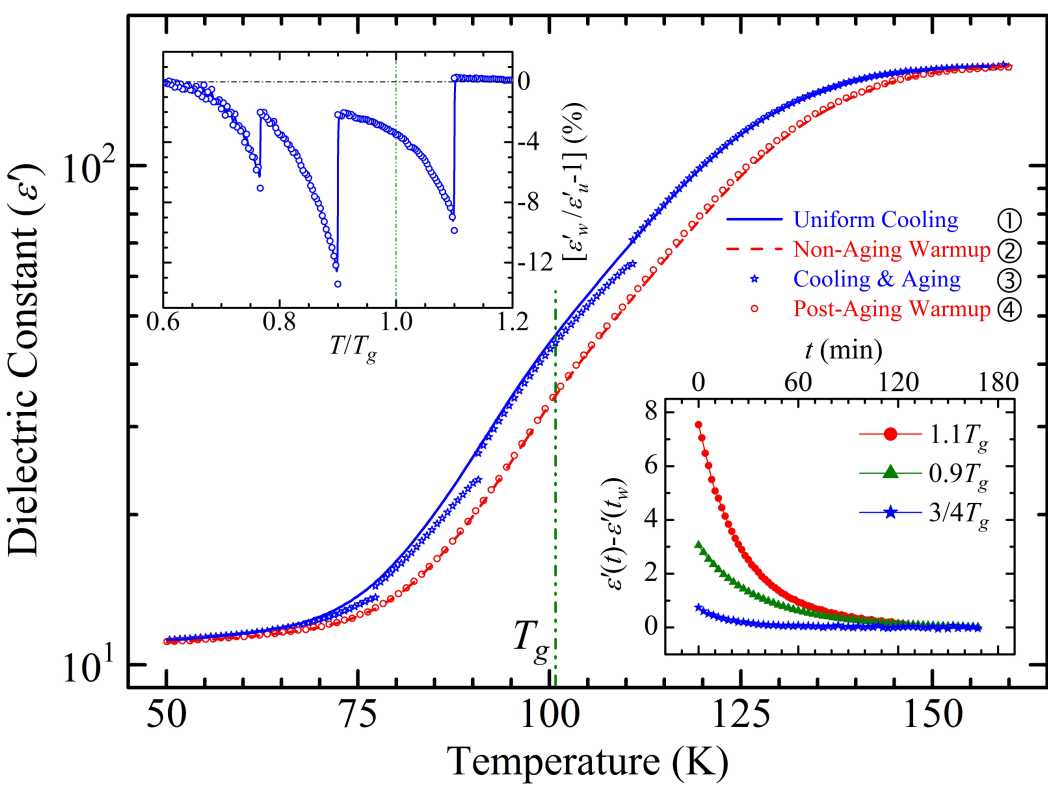
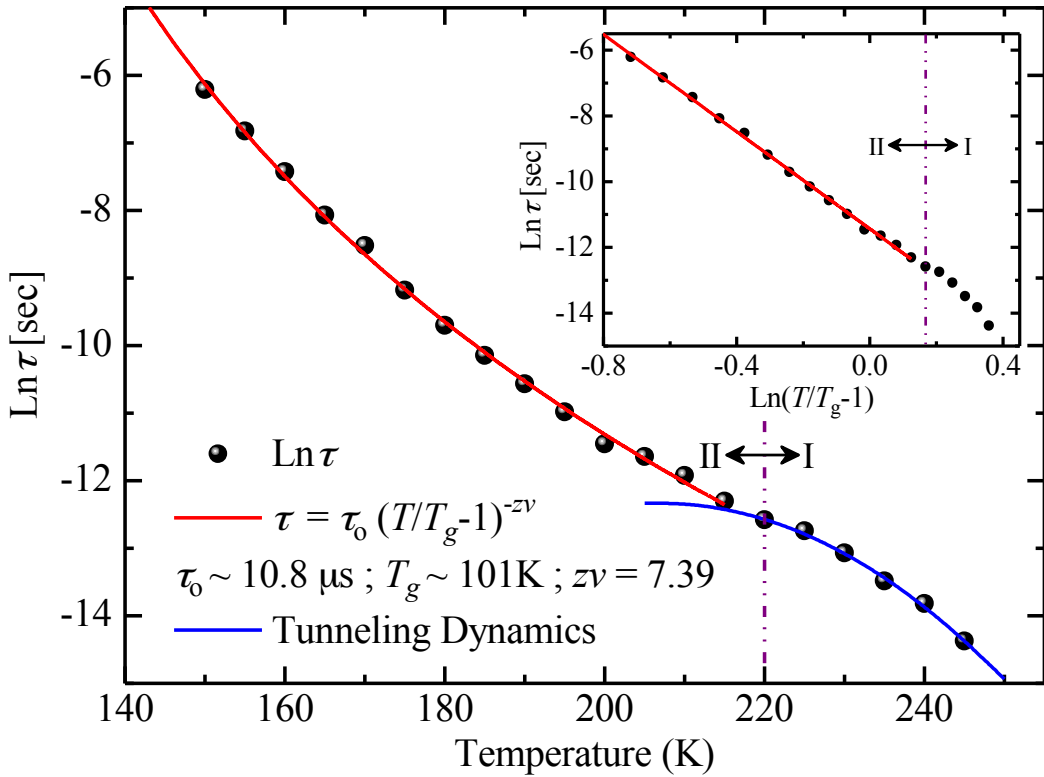


Fig. 3



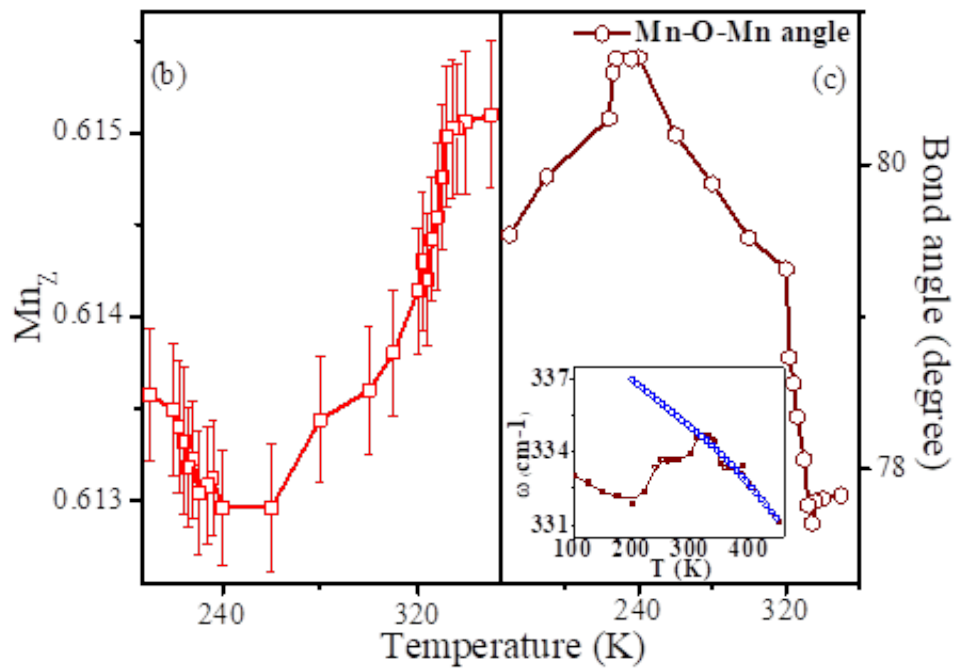
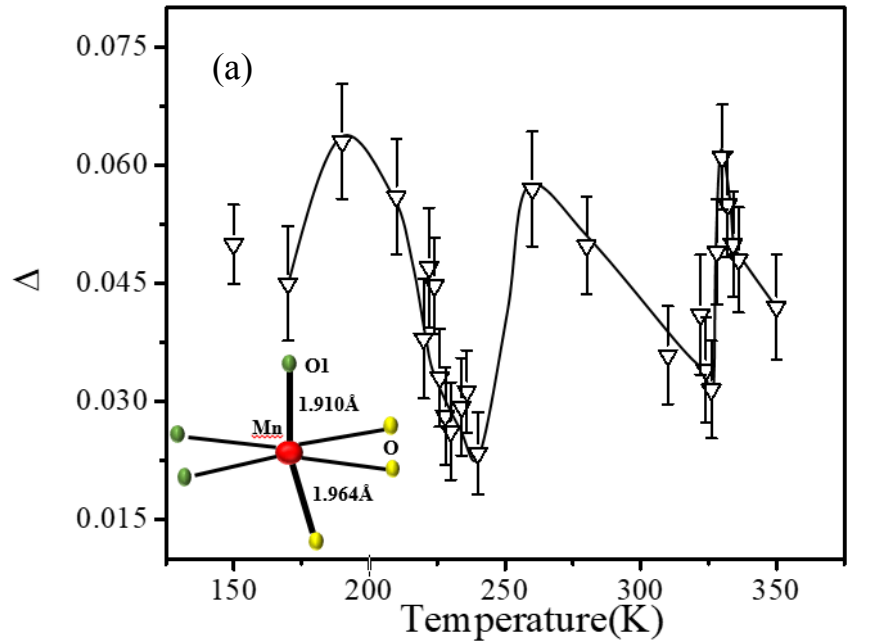


Fig 6

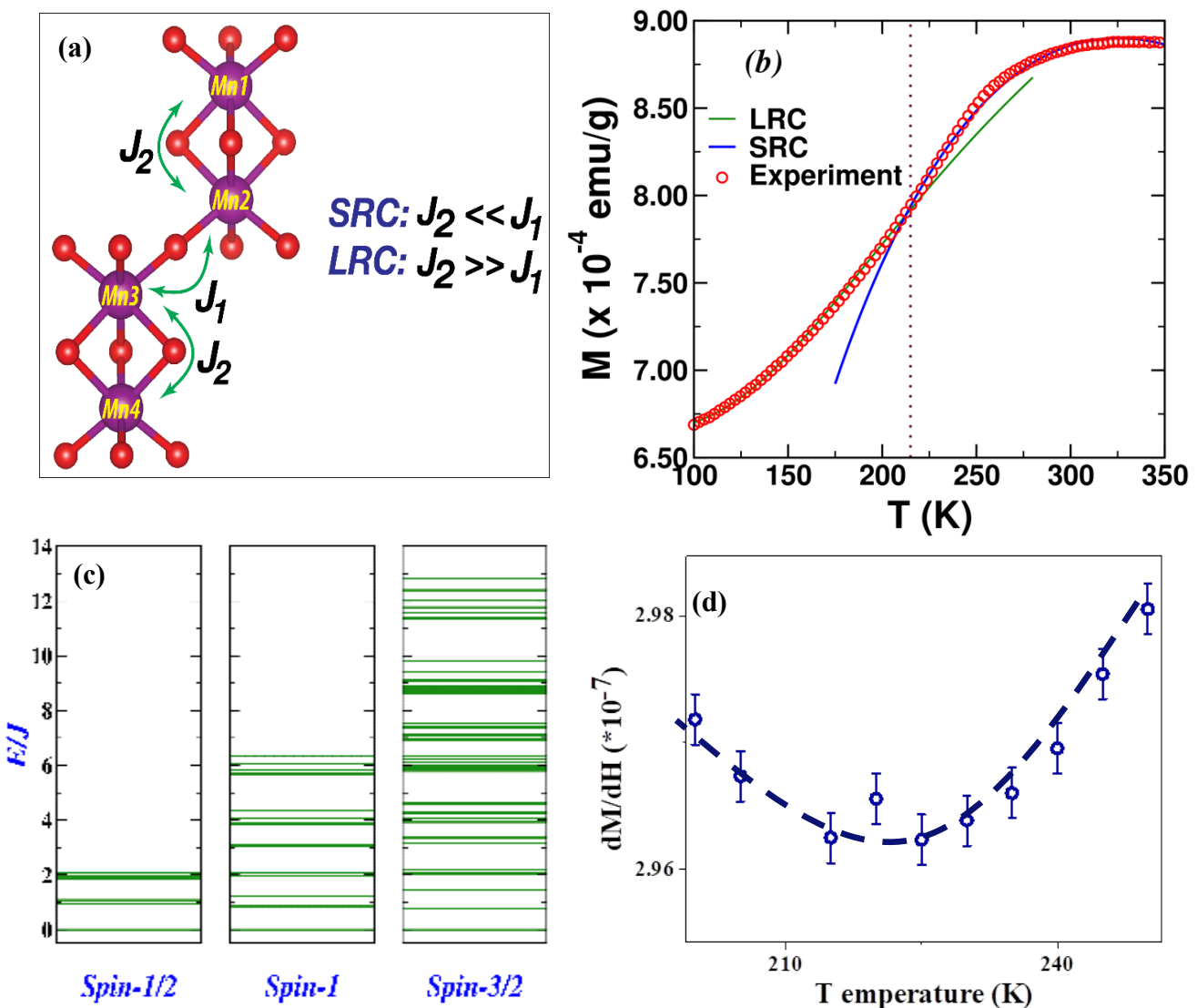


Fig 7

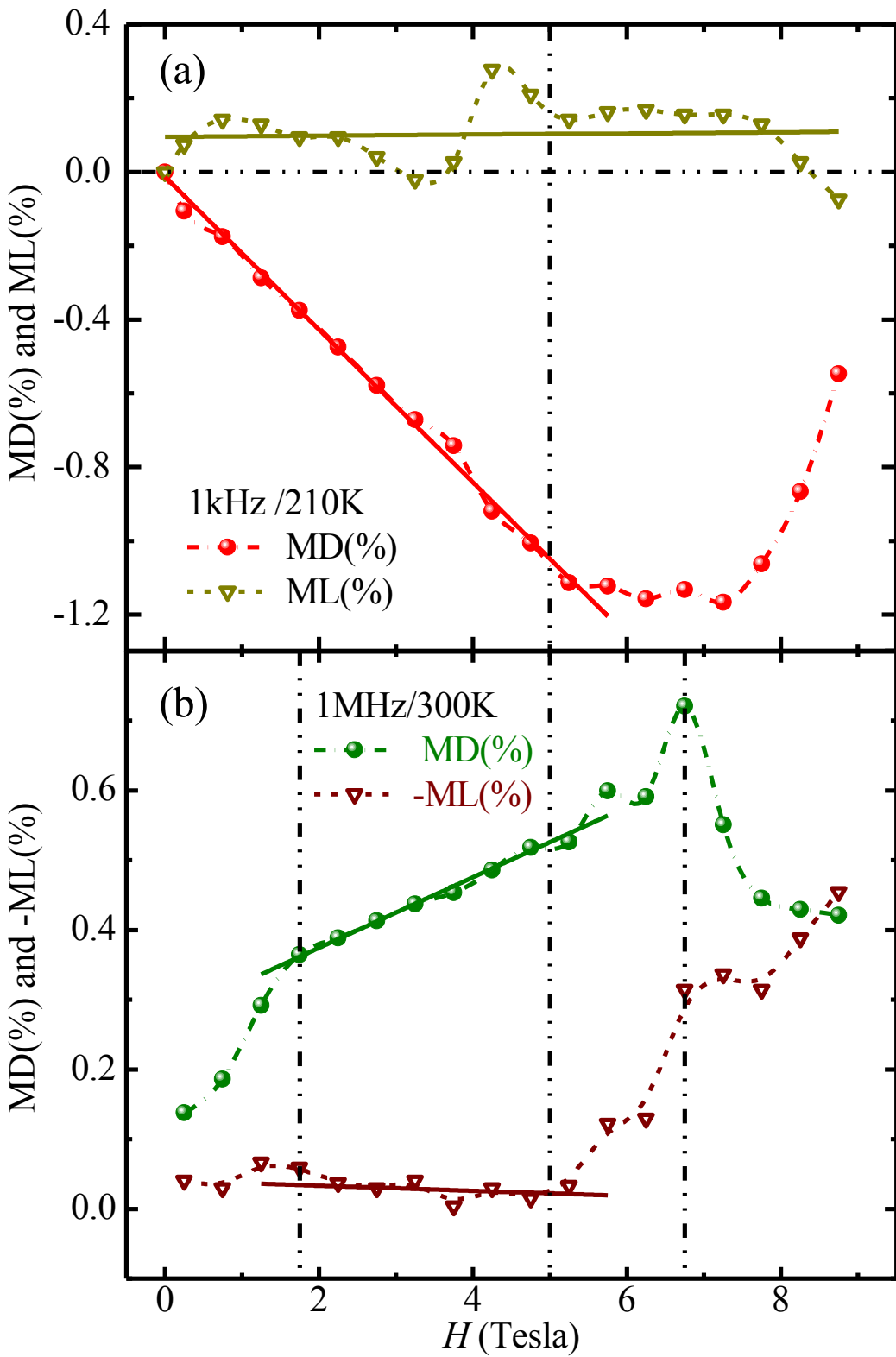


Fig 8